Spin–orbital-angular-momentum coupling in Bose-Einstein condensates

Kuei Sun, Chunlei Qu, and Chuanwei Zhang[*]

Department of Physics, The University of Texas at Dallas, Richardson, Texas 75080-3021, USA

Spin-orbit coupling (SOC) plays a crucial role in many branches of physics. In this context, the recent experimental realization of the coupling between spin and linear momentum of ultracold atoms opens a completely new avenue for exploring new spin-related superfluid physics. Here we propose that another important and fundamental SOC, the coupling between spin and orbital angular momentum (SOAM), can be implemented for ultracold atoms using higher-order Laguerre-Gaussian laser beams to induce Raman coupling between two hyperfine spin states of atoms. We study the ground-state phase diagrams of SOAM-coupled Bose-Einstein condensates on a ring trap and explore their applications in gravitational force detection. Our results may provide the basis for further investigation of intriguing superfluid physics induced by SOAM coupling, such as collective excitations.

PACS number(s): 03.75.Mn, 37.10.Vz, 67.85.−d

I. INTRODUCTION

Spin-orbit coupling (SOC), the interaction between a particle's spin and orbital degrees of freedom, takes place in nature in various ways. For a relativistic spinor, its spin angular momentum naturally couples to the linear momentum under Lorentz transformation, constituting the key physics in the Dirac equation [1]. In solid-state systems, the spin and linear momentum (SLM) coupling (e.g., Rashba [2] and Dresselhaus [3] coupling) is crucial for many important phenomena such as quantum spin Hall effects [4–7], topological insulators, and topological superconductors [8,9]. Recently, a highly tunable SLM coupling has been realized in cold atom experiments [10–20] using Raman coupling between two atomic hyperfine states [21]. These experimental advances have resulted in an active field of experimental and theoretical study [22–48] on the physics of SLM coupled Bose-Einstein condensates (BECs) and degenerate Fermi gases.

Another ubiquitous SOC in atomic and condensed matter physics is the coupling between spin and orbital angular momentum (SOAM). In a hydrogen atom, the electron's orbital movement generates a magnetic moment that couples to its spin, leading to SOAM coupling that is responsible for the spectroscopic fine structure. In solid-state systems, SOAM coupling plays a crucial role for magnetic properties of materials [49,50]. However, the SOAM coupling for ultracold atoms has not been realized in experiments and the physics of SOAM-coupled BEC and degenerate Fermi gases has not been well explored.

In this paper we propose a practical scheme for generating SOAM coupling for cold atoms and investigate the ground-state properties of SOAM-coupled BEC. Our main results are the following:

(1) We propose that the SOAM coupling for cold atoms can be realized using two copropagating Laguerre-Gaussian (LG) laser beams [51–56] that couple two atomic hyperfine states through the two-photon Raman process [57,58] [see Fig. 1(a)]. Note that only the lowest-order Gaussian laser beams have been used in the implementation of SLM coupling, and

―――――
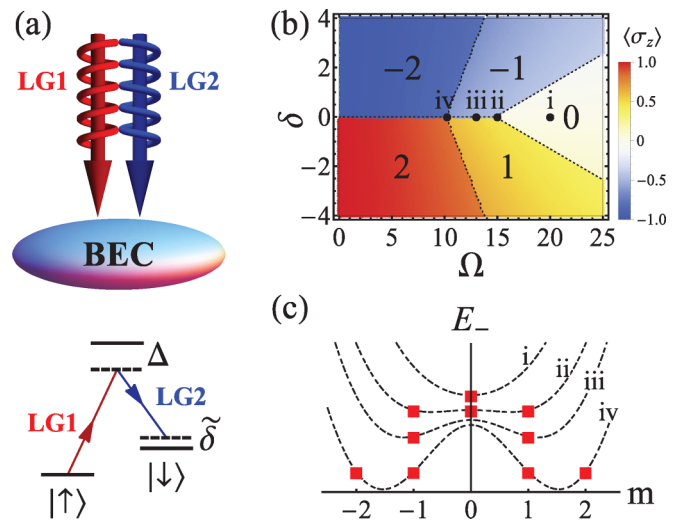[*]Corresponding author: chuanwei.zhang@utdallas.edu

FIG. 1. (Color online) (a) Two copropagating LG beams with different OAM-coupled two internal states of a BEC through the Raman transition. (b) Noninteracting ground-state phase diagram for $l = 2$ in the plane of detuning δ and Raman coupling Ω. The ground-state OAM quantum numbers are labeled in corresponding blocks separated by dashed lines. The colors scaled in bar graph represent spin polarization $\langle\sigma_z\rangle$. (c) The ground states (filled squares) and the assumed continuous spectra (dashed curves) at selected points in panel (b). (i) Single ground state $|0\rangle$; (ii) threefold degeneracy $|0\rangle$, $|\pm 1\rangle$ at $\Omega_c = 15$; (iii) twofold degeneracy $|\pm 1\rangle$; and (iv) fourfold degeneracy $|\pm 1\rangle$, $|\pm 2\rangle$. The curves are arbitrarily shifted in $\hat{y}$ direction.

higher-order LG laser beams are widely available in optical and atomic experiments. We derive the single-particle Hamiltonian with SOAM coupling as a function of the laser parameters.

(2) We study the ground-state properties of a SOAM-coupled BEC trapped on a ring. This geometry has been recently realized in experiments [59–61]. We find that the interplay between SOAM coupling and orbital angular momentum (OAM) quantization can lead to fourfold degenerate ground states and first-order transitions between different OAM phases. Both have not been found in the SLM-coupled BEC. We also find strongly interacting effects in the system,

including a significant deviation from the single-particle picture and a very large stripe-phase region.

(3) We show that inhomogeneous potentials, such as gravitational potentials, can induce the mixture of neighboring OAM states, leading to the transition from uniform to stripe types of density distributions. Such a transition may find potential applications in designing gravitational force detection devices.

The paper is organized as follows. In Sec. II we derive the model Hamiltonian with SOAM coupling. We then analyze the single-particle physics of a ring system in Sec. III and show interacting phase diagrams for a realistic ring BEC in Sec. IV. In Sec. V we study effects of external potentials. Experimental parameters are discussed in Sec. VI. Section VII is the Conclusion.

II. MODEL AND HAMILTONIAN

As illustrated in Fig. 1(a), we consider an atomic BEC with two internal spin states, $|\uparrow\rangle$ and $|\downarrow\rangle$, coupled by a pair of copropagating Raman lasers. In order to transfer OAM from the laser to atoms, both Raman lasers are chosen to be LG beams with different OAM denoted by azimuthal indices $l_{1,2}$, respectively. The one-photon Rabi frequency from the jth beam in cylindrical coordinate can be written as

$$\Omega_j(\mathbf{r}) = \Omega_{0,j} \left(\frac{\sqrt{2}r}{w} \right)^{|l_j|} \exp\left(-\frac{r^2}{w^2} + il_j\phi + ik_z z \right), \quad (1)$$

where $\Omega_{0,j}$ is proportional to the beam intensity, w is the beam waist, r is the radius, and ϕ is the azimuthal angle. Hereafter we consider the case $-l_1 = l_2 = l$ for convenience. The two-photon Raman coupling between two spin states is $\Omega_1 \bar{\Omega}_2 / 4\Delta \equiv (\tilde{\Omega}/2) f(r) e^{-2il\phi}$, with the strength $\tilde{\Omega}$ and spatial distribution $f(r)$. Incorporating additional detuning $\tilde{\delta}/2$, the effective single-particle Hamiltonian is written as

$$H_0 = \begin{pmatrix} -\frac{\hbar^2 \nabla^2}{2M} + \frac{\tilde{\delta}}{2} & \frac{\tilde{\Omega}}{2} f e^{-2li\phi} \\ \frac{\tilde{\Omega}}{2} f e^{2li\phi} & -\frac{\hbar^2 \nabla^2}{2M} - \frac{\tilde{\delta}}{2} \end{pmatrix} + V(r), \quad (2)$$

in basis $\Psi = (\psi_\uparrow, \quad \psi_\downarrow)^T$, where $V(r) = \text{diag.}(|\Omega_1|^2/4\Delta, |\Omega_2|^2/4\Delta)$ describes the Stark shift [51] and M is the atomic mass. After a unitary transformation $\psi_{\uparrow/\downarrow} \to e^{\mp il\phi}\psi_{\uparrow/\downarrow}$, we obtain

$$H_0' = \frac{\hbar^2}{2Mr^2} \left[-(r\,\partial_r)^2 + \left(\frac{L_z}{\hbar}\right)^2 - 2l\left(\frac{L_z}{\hbar}\right)\sigma_z + l^2 \right]$$
$$- \frac{\hbar^2 \partial_z^2}{2M} + \frac{\tilde{\Omega}}{2} f(r)\sigma_x + \frac{\tilde{\delta}}{2}\sigma_z + V(r), \quad (3)$$

where $L_z = -i\hbar\partial_\phi$ is the z component of the angular momentum operator and $\{\sigma_j\}$ are Pauli matrices. The SOAM coupling $L_z\sigma_z$ (as a part of more general $\mathbf{L} \cdot \boldsymbol{\sigma}$ coupling) emerges from such transformation, similar to the appearance of $k_x\sigma_z$ in SLM coupling experiments [10–20].

III. RING SYSTEM

To reveal the most salient effects of SOAM coupling in both theoretical and experimental aspects, we investigate a ring BEC with a fixed radius R. Integrating out the z and r

dependence and using the natural energy unit $\epsilon = \hbar^2/(2MR^2)$, we turn Eq. (3) into a dimensionless ring Hamiltonian,

$$H_0^{\text{ring}} = -\partial_\phi^2 + \left(2il\partial_\phi + \frac{\delta}{2} \right)\sigma_z + \frac{\Omega}{2}\sigma_x, \quad (4)$$

where $\delta = \tilde{\delta}/\epsilon$ and $\Omega = \tilde{\Omega}f(R)/\epsilon$ are the dimensionless detuning and Raman coupling, respectively. Because $[H_0^{\text{ring}}, L_z] = 0$, the eigenstates of H_0^{ring} coincide with the OAM eigenstates $|m\rangle$, or $e^{im\phi}$ with an integer m. The energy spectrum shows two bands with the lowest one

$$E_-(m) = m^2 - \frac{1}{2}\sqrt{(4lm - \delta)^2 + \Omega^2}. \quad (5)$$

Applying the Hellmann-Feynman theorem, one can compute the spin polarization from the energy spectrum as $\langle\sigma_z\rangle = \partial E_-/\partial(\delta/2)$ and $\langle\sigma_x\rangle = \partial E_-/\partial(\Omega/2)$.

For an assumed continuous spectrum, the ground state would correspond to a real number m^*, analogous to the SLM coupling case. In our system, however, due to OAM quantization, the ground state does not exactly lie at m^* but the nearest integer(s) $[m^*]$. Therefore, there can be two degenerate ground states with adjacent quantum numbers (reminiscent of a recently proposed idea of quantum time crystal [62]). By letting $E_-(m) = E_-(m + 1)$, we obtain a condition for degenerate $|m\rangle$ and $|m + 1\rangle$ as $q_m\Omega = \sqrt{(4l^2 - q_m^2)[(2lq_m - \delta)^2 - q_m^2]}$ with $q_m = 2m + 1$. If $\delta = 0$, the system has another two-fold degeneracy $|\pm m\rangle$, except for $m = 0$. Combining these conditions, the noninteracting case can exhibit at most fourfold degeneracy $|\pm m\rangle$ and $|\pm(m + 1)\rangle$. On the other hand, in the large Ω limit, the system always has a single ground state $|0\rangle$. The double-minimum structure of $|\pm m\rangle$ degeneracy appears as Ω decreases across a critical value Ω_c, which can be evaluated as a threefold degeneracy point of $|0\rangle$ and $|\pm 1\rangle$. We hence obtain $\Omega_c = 4l^2 - 1$. This is different from a continuous spectrum because of the quantization of m. When double minima appear at $\pm m^*$ closer to 0 than 1, the system is enforced in the single state $|0\rangle$.

In Fig. 1(b) we plot the ground-state phase diagram for $l = 2$. The OAM quantum numbers m are labeled on the corresponding blocks with borders in dashed lines, which also represent regions with degeneracy. The spin polarization $\langle\sigma_z\rangle$ displays discontinuity with the change of m, and its sign is locked with the sign of m for any nonzero m. Both signatures can be directly attributed to the presence of SOAM coupling. In Fig. 1(c), we label the ground state(s) on the assumed continuous spectrum at selected points along the $\delta = 0$ line. We see the transition from nondegenerate to various multidegenerate ground states as Ω varies. Remarkably, the threefold (curve ii) and fourfold (iv) degeneracy does not occur in the continuous spectrum.

IV. INTERACTION EFFECTS

We now analyze realistic systems with s-wave scattering interactions. Incorporating the interactions $g_\uparrow$ ($g_\downarrow$) between up (down) bosons and the interspin boson $g_\updownarrow$, the system's energy reads as

$$E = \int_0^{2\pi} \Psi^\dagger \left(H_0^{\text{ring}} + H_g^{\text{ring}} \right)\Psi \, d\phi, \quad (6)$$

where

$$H_g^{\text{ring}} = \frac{1}{2}\begin{pmatrix} g_\uparrow \bar\psi_\uparrow \psi_\uparrow & g_\updownarrow \bar\psi_\downarrow \psi_\uparrow \\ g_\updownarrow \bar\psi_\uparrow \psi_\downarrow & g_\downarrow \bar\psi_\downarrow \psi_\downarrow \end{pmatrix}. \qquad (7)$$

The normalization condition is set as $\int_0^{2\pi} \Psi^\dagger \Psi \, d\phi = 1$ such that $g_{\uparrow,\downarrow,\updownarrow}$ are proportional to the total number of particles N.

To capture the effects of SOAM coupling, interactions, and possible degeneracies, we adopt a variational wave function of the form

$$\Psi = (\Psi_1 + e^{i\zeta} \Psi_2)/\sqrt{2\pi}, \qquad (8)$$

where

$$\Psi_j = |C_1^j| \begin{pmatrix} \cos\theta_j \\ -\sin\theta_j \end{pmatrix} e^{i(m_j\phi + \eta_j)}$$

$$+ |C_2^j| \begin{pmatrix} \sin\theta_j \\ -\cos\theta_j \end{pmatrix} e^{-i(m_j\phi + \eta_j)}, \qquad (9)$$

with $m_1 = m$ and $m_2 = m + 1$. The normalization condition gives $\sum_{i,j} |C_i^j|^2 = 1$. The range of parameters is set to be $0 \leqslant \theta_j \leqslant \pi/2$ and $-\pi \leqslant \eta_j, \zeta < \pi$. With this ansatz, we obtain E as a function of six independent parameters $|C_1^1|, |C_1^2|, |C_2^1|$, θ_1, θ_2, and ζ. The two phases η_1 and η_2 do not affect E here but can play a role in a general case with external potentials. These parameters are determined through the minimization of E. In addition, we compare the variational results with those from solving the Gross-Pitaevskii equation (GPE) by the imaginary time evolution and find good agreement between them.

With the interactions on, we obtain either $\Psi_1 = 0$ or $\Psi_2 = 0$, which indicates energetic disfavor of the superposition of $|m\rangle$ and $|m+1\rangle$. As a result, $\langle|m|\rangle$ is always an integer and the phase ζ plays no role. Below we assume $\Psi_2 = 0$ for convenience.

Figures 2(a) and 2(b) show phase diagrams for $l = 2$ at a fixed ratio $g_\downarrow = g_\updownarrow = 0.9954 g_\uparrow$. We present quantum numbers, phase boundary, and spin polarization in the same convention as Fig. 1(b). The gray dashed curves in panel (a) show the noninteracting phase boundary for comparison. We see that the presence of interaction leads to (1) an emerging stripe phase and (2) phase boundary shifts. In regions denoted with integer m, the ground state lies in this specific quantum number, which means only one of $|C_1^1|$ and $|C_2^1|$ is nonzero, or $|C_1^1 C_2^1| = 0$. Similar to the SLM coupling case, there appears a region showing $|C_1^1 C_2^1| \neq 0$, corresponding to a linear combination of $|\pm m\rangle$ (denoted by S_m). This state exhibits a spatial modulation in particle density or a stripe structure, since $\Psi^\dagger \Psi = 1 + 2|C_1^1 C_2^1| \sin 2\theta_1 \cos 2(m\phi + \eta_1)$. The net spin polarization $\langle \sigma_z \rangle$ is strongly suppressed in the stripe phase due to the cancellation from $|\pm m\rangle$ with opposite polarizations. In contrast to the SLM coupling case, the stripe phase here can still exhibit significant spin polarization as a function of the detuning.

In panel (a), the vertical shifts of the phase boundary come from the asymmetry of the interactions $g_\uparrow \neq g_\downarrow$, which causes an effective Zeeman splitting $(g_\uparrow - g_\downarrow)/8\pi \times \langle \sigma_z \rangle$ in the energy functional. This interaction-induced splitting, which energetically favors down spins, competes with the detuning $\delta/2$ in its negative region. The phase boundary
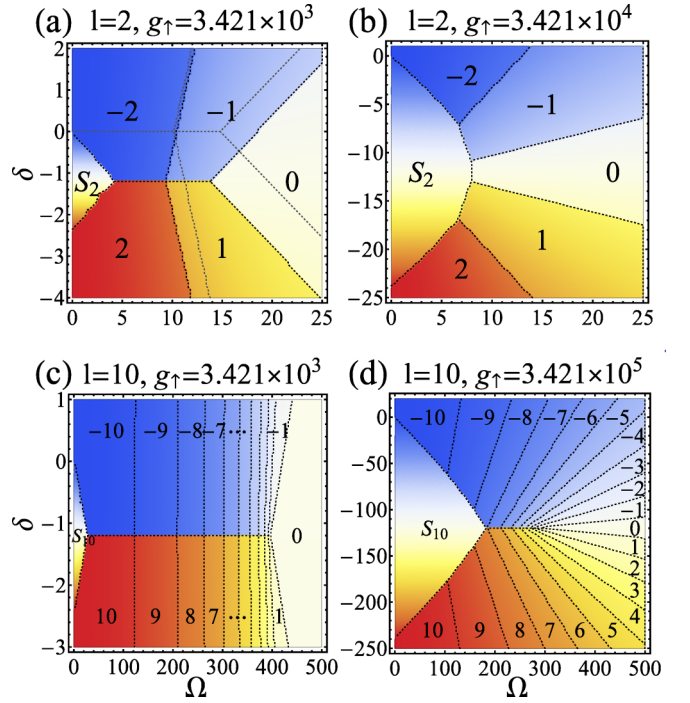

FIG. 2. (Color online) Phase diagrams with the presence of interactions. (a) [(b)] corresponds to $l = 2$ and $g_\uparrow = 3.421 \times 10^3$ (10^4), and (c) [(d)] does to $l = 10$ and $g_\uparrow = 3.421 \times 10^3$ (10^5). We set $g_\downarrow = g_\updownarrow = 0.9954 g_\uparrow$, which is good for ^{87}Rb atoms. In (a) the noninteracting boundaries are drawn in gray dashed lines for comparison. Conventions are the same as Fig. 1(b), except an emerging stripe phase as a combination of $|\pm m\rangle$ is denoted by S_m.

between $|\pm m\rangle$ and the zero polarization line of the stripe phase hence vertically shifts to a point $\delta \sim -(g_\uparrow - g_\downarrow)/4\pi$ where the two effects balance. As $g_\uparrow$ increases by an order [from (a) to (b)], the stripe phase S_2 expands, invades the single-m region, and finally intersects with all m phases. At intermediate stages, the boundary of S_2 can meet the point of degenerate $|\pm 1\rangle, |\pm 2\rangle$ to form a fivefold degeneracy and meet Ω_c (point of degenerate $|0\rangle, |\pm 1\rangle$) to form a fourfold degeneracy. We notice that the S_1 phase is never energetically favorable here. In addition, we find that Ω_c decreases with the increase in $g_\uparrow$, indicating an interaction-induced change between the single- and double-minimum structures [13,32].

For a larger l case, the structure of the phase diagram remains the same: the stripe phase on the left, $m \geqslant 1$ phases decreasing from $|m| = l$ to $|m| = 1$ in the middle, and $m = 0$ phase on the right. Panels (c) and (d) are phase diagrams for a case of higher-order LG beams with $l = 10$. In (c) we see the same structure as the $l = 2$ case in (a). The stripe phase S_{10} appears on the left between $-2.4 < \delta < 0$, while the zero momentum phase $|0\rangle$ appears on the right. In the middle region, the finite quantum number phases $|m\rangle$ monotonically decrease from $m = 10$ to $m = 1$ if $\delta < -1.2$, while m changes sign if $\delta > -1.2$. The magnitude and sign of $\langle \sigma_z \rangle$ behave in the same trend as m. In (d) we show strongly interacting effects by increasing the interaction strength by 100 times. One sees that the stripe-phase region significantly expands, the boundaries of single-m phases become more inclined, and the
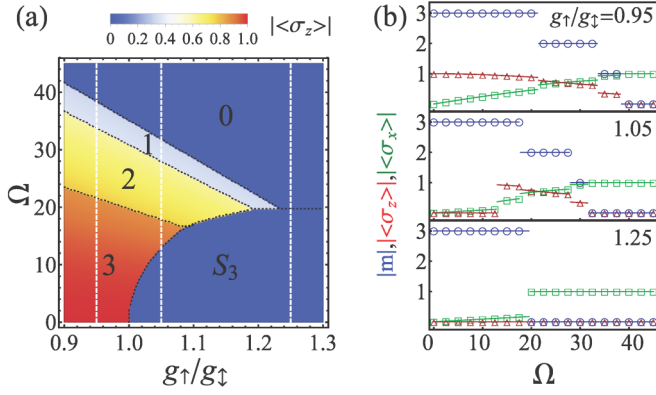
FIG. 3. (Color online) (a) Phase diagram in the Ω–$(g_\uparrow/g_\updownarrow)$ plane. The $|m\rangle$ phases labeled by $|m|$ and the stripe phase S_3 are separated by dashed lines. The colors represent spin polarization magnitude $|\langle\sigma_z\rangle|$ scaled in the bar graph. The parameters are $l = 3, \delta = 0, g_\uparrow = g_\downarrow$, and $g_\updownarrow = 424$ (good for ^{23}Na atoms). (b) From top to bottom: quantum number $|m|$ (circles) and spin polarizations $|\langle\sigma_z\rangle|$ (triangles) as well as $|\langle\sigma_x\rangle|$ (squares) vs Ω at $g_\uparrow/g_\updownarrow = 0.95, 1.05$, and 1.25, respectively, corresponding to the white dashed lines in (a).

FIG. 4. (Color online) (a) Expectation value $\langle m\rangle$ (circles, axis on left) and density contrast [triangles, axis on right of (b)] vs Ω at gravity strength $V_G = 0.05$ in a noninteracting system. The dashed curve shows $\langle m\rangle$ at $V_G = 0$ for comparison. Insets: normalized ring density profiles (scaled in bar graph) for the two cases at $\Omega = 10.25$, indicated by the arrows, respectively. (b) Same quantities vs V_G at $\Omega = 10$ and $g_\uparrow = g_\downarrow = g_\updownarrow = 100$.

zero-momentum-phase region shrinks. Such a trend is similar to the $l = 2$ case in (a) and (b).

We turn to study a case where the ratio of intraspin and interspin interactions varies. Figure 3(a) shows a phase diagram as a function of Ω and $g_\uparrow/g_\updownarrow$, given $g_\uparrow = g_\downarrow$, $g_\updownarrow = 424$, $l = 3$, and $\delta = 0$. We see that the stripe phase S_3 exists only when the ratio $g_\uparrow/g_\updownarrow > 1$ and $m \geqslant 1$ phases disappear at large ratio. In Fig. 3(b) we plot $|m|$, $|\langle\sigma_z\rangle|$, and $|\langle\sigma_x\rangle|$ vs Ω at $g_\uparrow/g_\updownarrow = 0.95$ (no stripe phase), 1.05 (all phases), and 1.25 (no finite-m phase), corresponding to the white dashed lines from left to right in Fig. 3(a), respectively. We see that the system finally becomes fully polarized in $\langle\sigma_x\rangle$ at large Ω. The discrete jumps of $\langle\sigma_x\rangle = \partial E/\partial\Omega$ indicate first-order phase transitions between stripe and nonstripe phases, as well as between different m phases.

V. EXTERNAL POTENTIAL

We consider effects of a gravitational potential $M a_g R \sin\alpha\cos\phi$, where a_g is the gravitational acceleration and α is the angle between the ring plane and the horizontal plane. For the mass of ^{23}Na, $R = 8$ μm, we obtain a dimensionless gravity strength $V_G \equiv M a_g R \sin\alpha/\epsilon = 1315\sin\alpha$, comparable to the interaction strength as shown later. The gravity couples two adjacent OAM states because $\langle m|\cos\phi|m \pm 1\rangle = \frac{1}{2}\langle m|e^{i\phi} + e^{-i\phi}|m \pm 1\rangle \neq 0$, so it should play a crucial role when the two states are nearly degenerate. In such a case the variational ground state can have both Ψ_1 and Ψ_2 nonzero. To pinpoint this effect, we first study the transition region between $m = 1$ and 2 in the noninteracting case with tiny detuning [along the $\delta = -0.01$ line in Fig. 1(b)]. We plot $\langle m\rangle$ and density contrast (defined as the normalized difference $\frac{\rho_M - \rho_m}{\rho_M + \rho_m}$ between density maximum ρ_M and minimum ρ_m) vs Ω at $V_G = 0.05$ in Fig. 4(a). In contrast to the discontinuity of the $V_G = 0$ case (dashed curve), $\langle m\rangle$ at $V_G = 0.05$ goes smoothly from 2 to 1, indicating a mixed state around the transition point $\Omega = 10.25$. Such a state exhibits an inhomogeneous density
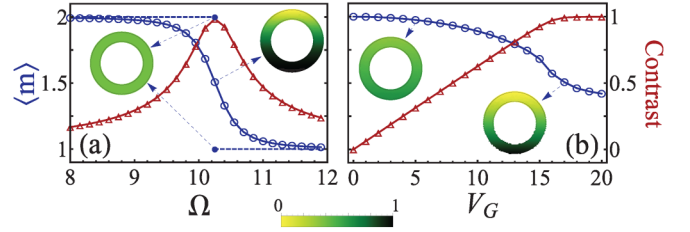
profile (i.e., a stripe) that is qualitatively different from the uniform one at $V_G = 0$ (see inset). This makes the system a very sensitive detector for gravity ($V_G = 0.05$ corresponds to $\alpha \lesssim 10^{-4}$). Figure 4(b) shows the same quantities vs V_G at $\Omega = 10$, $g_\uparrow = g_\downarrow = g_\updownarrow = 100$, and $\delta = 0$, obtained from GPE. (The variational results deviate at large V_G due to the truncation of the Hilbert space.) The contrast linearly increases with V_G and saturates when $V_G > 16$. The sensitivity is hence controllable through the tuning of Ω and the interactions.

Another experimentally feasible potential is an anisotropic trapping $\frac{1}{2}m\omega^2[x^2 + (1 - \lambda^2)y^2] = \frac{1}{4}m\omega^2 R^2\lambda^2\cos 2\phi$ up to a constant. This potential couples $|m\rangle$ and $|m \pm 2\rangle$ and is expected to stabilize the stripe phase composed of $|\pm 1\rangle$. The gravity and anisotropic trapping are also capable of inducing dipole and quadrupole density oscillations, respectively, for studying the ring's collective excitations.

VI. EXPERIMENTAL ASPECTS

For a ^{87}Rb gas trapped in a ring of radius $R = 20$ μm and thickness $b = 5$ μm [59,60], we have $\epsilon = 2\pi\hbar \times 0.145$ Hz. The dimensionless interaction strength can be evaluated as $g = 8NRa_s/b^2$ with the two-body scattering length a_s [63,64]. The intraspin and interspin scattering lengths fix the ratio $g_\downarrow = g_\updownarrow = 0.9954 g_\uparrow$ [10]. For $a_s = 100.86a_0$ (Bohr radius) and $N = 10^5$, we obtain $g_\uparrow = 3.421 \times 10^3$ (as used in Fig. 2). One can enhance ϵ to $2\pi\hbar \times 0.91$ Hz by shrinking the ring size to $R = 8$ μm, which, combined with higher-order LG beams of $l = 10$ [65], gives $\Omega_c = 2\pi\hbar \times 363$ Hz. For a ^{23}Na gas [66] with $R = 8$ μm and $l = 10$, we get $\epsilon = 2\pi\hbar \times 3.43$ Hz and $\Omega_c = 2\pi\hbar \times 1369$ Hz. Given $b = 2$ μm, $N = 10^4$, and $a_s = 50$ a_0, typical interaction strength is equal to 424 ϵ (as used in Fig. 3). For typical $\Omega \simeq 1$ kHz, the heating effect due to spontaneous photon emission of Raman lasers should be weak for a typical experimental time scale of 1 s [33]. We notice that, because ϵ can be so small, the interaction energy $[O(g/2\pi)]$ can be much larger than the kinetic energy $[O(l)]$ and even Ω_c. Therefore, unlike the current ^{87}Rb platform where interactions show little competition with the SLM coupling, our ring system is instead suited for exploring the strongly interacting regime, where the ground-state phase diagram could be significantly different from the noninteracting case. For experimental detection, the quantum number m corresponding to a superfluid

winding number can be determined by absorption images of the BEC after time-of-flight (TOF) expansion [60]. The stripe phase will maintain its pattern during TOF [65]. Finally, we note that there is ongoing experimental effort for generating such SOAM coupling using ^{87}Rb atoms confined on a ring trap [67].

VII. CONCLUSION

A realistic scheme for generating SOAM coupling in cold atom gases is proposed and analyzed. Study of the ground-state phase diagram of the SOAM-coupled BEC on a ring reveals the strong effects of many-body interaction

with the currently experimentally available parameters. The results should provide a new platform for exploring SOAM-coupled cold atomic physics for both bosons and fermions. Generalization of the scheme for the full $\boldsymbol{L} \cdot \boldsymbol{\sigma}$ coupling may involve more LG laser beams and additional hyperfine states, but may bring new exotic physics.

[1] P. A. M. Dirac, The quantum theory of the electron, Proc. R. Soc. Lond. A **117**, 610 (1928).

[2] E. I. Rashba, Properties of semiconductors with an extremum loop. 1. Cyclotron and combinational resonance in a magnetic field perpendicular to the plane of the loop, Sov. Phys. Solid State **2**, 1109 (1960); Y. A. Bychkov and E. I. Rashba, Oscillatory effects and the magnetic susceptibility of carriers in inversion layers, J. Phys. C **17**, 6039 (1984).

[3] G. Dresselhaus, Spin-orbit coupling effects in zinc blende structures, Phys. Rev. **100**, 580 (1955).

[4] Y. K. Kato, R. C. Myers, A. C. Gossard, and D. D. Awschalom, Observation of the spin Hall effect in semiconductors, Science **306**, 1910 (2004).

[5] C. L. Kane and E. J. Mele, Z_2 topological order and the quantum spin Hall effect, Phys. Rev. Lett. **95**, 146802 (2005).

[6] M. König, S. Wiedmann, C. Brüne, A. Roth, H. Buhmann, L. W. Molenkamp, X.-L. Qi, and S.-C. Zhang, Quantum spin Hall insulator state in HgTe quantum wells, Science **318**, 766 (2007).

[7] B. A. Bernevig, T. L. Hughes, and S.-C. Zhang, Quantum spin Hall effect and topological phase transition in HgTe quantum wells, Science **314**, 1757 (2006).

[8] M. Z. Hasan and C. L. Kane, Colloquium: Topological insulators, Rev. Mod. Phys. **82**, 3045 (2010).

[9] X.-L. Qi and S.-C. Zhang, Topological insulators and superconductors, Rev. Mod. Phys. **83**, 1057 (2011).

[10] Y.-J. Lin, K. Jiménez-García, and I. B. Spielman, Spin-orbit-coupled Bose-Einstein condensates, Nature (London) **471**, 83 (2011).

[11] J.-Y. Zhang, S.-C. Ji, Z. Chen, L. Zhang, Z.-D. Du, B. Yan, G.-S. Pan, B. Zhao, Y.-J. Deng, H. Zhai, S. Chen, and J.-W. Pan, Collective dipole oscillations of a spin-orbit coupled Bose-Einstein condensate, Phys. Rev. Lett. **109**, 115301 (2012).

[12] C. Qu, C. Hamner, M. Gong, C. Zhang, and P. Engels, Observation of Zitterbewegung in a spin-orbit-coupled Bose-Einstein condensate, Phys. Rev. A **88**, 021604(R) (2013).

[13] C. Hamner, C. Qu, Y. Zhang, J. Chang, M. Gong, C. Zhang, and P. Engels, Dicke-type phase transition in a spin-orbit-coupled Bose–Einstein condensate, Nat. Commun. **5**, 4023 (2014).

[14] A. J. Olson, S.-J. Wang, R. J. Niffenegger, C.-H. Li, C. H. Greene, and Y. P. Chen, Tunable Landau-Zener transitions in a spin-orbit-coupled Bose-Einstein condensate, Phys. Rev. A **90**, 013616 (2014).

[15] S.-C. Ji, J.-Y. Zhang, L. Zhang, Z.-D. Du, W. Zheng, Y.-J. Deng, H. Zhai, S. Chen, and J.-W. Pan, Experimental determination of the finite-temperature phase diagram of a spin-orbit coupled Bose gas, Nat. Phys. **10**, 314 (2014).

[16] K. Jimenéz-García, L. J. LeBlanc, R. A. Williams, M. C. Beeler, C. Qu, M. Gong, C. Zhang, and I. B. Spielman, Tunable spin-orbit coupling via strong driving in ultracold-atom systems, Phys. Rev. Lett. **114**, 125301 (2015).

[17] D. L. Campbell, R. M. Price, A. Putra, A. Valdés-Curiel, D. Trypogeorgos, and I. B. Spielman, Itinerant magnetism in spin-orbit coupled Bose gases, arXiv:1501.05984.

[18] P. Wang, Z.-Q. Yu, Z. Fu, J. Miao, L. Huang, S. Chai, H. Zhai, and J. Zhang, Spin-orbit coupled degenerate Fermi gases, Phys. Rev. Lett. **109**, 095301 (2012).

[19] L. W. Cheuk, A. T. Sommer, Z. Hadzibabic, T. Yefsah, W. S. Bakr, and M. W. Zwierlein, Spin-injection spectroscopy of a spin-orbit coupled Fermi gas, Phys. Rev. Lett. **109**, 095302 (2012).

[20] R. A. Williams, M. C. Beeler, L. J. LeBlanc, K. Jiménez-García, and I. B. Spielman, Raman-induced interactions in a single-component Fermi gas near an s-wave Feshbach resonance, Phys. Rev. Lett. **111**, 095301 (2013).

[21] I. B. Spielman, Raman processes and effective gauge potentials, Phys. Rev. A **79**, 063613 (2009).

[22] J. Dalibard, F. Gerbier, G. Juzeliūnas, and P. Öhberg, Colloquium: Artificial gauge potentials for neutral atoms, Rev. Mod. Phys. **83**, 1523 (2011).

[23] V. Galitski and I. B. Spielman, Spin-orbit coupling in quantum gases, Nature (London) **494**, 49 (2013).

[24] X. Zhou, Y. Li, Z. Cai, and C. Wu, Unconventional states of bosons with the synthetic spin-orbit coupling, J. Phys. B: At. Mol. Opt. Phys. **46**, 134001 (2013).

[25] N. Goldman, G. Juzeliūnas, P. Öhberg, and I. B. Spielman, Light-induced gauge fields for ultracold atoms, Rep. Prog. Phys. **77**, 126401 (2014).

[26] C. Wang, C. Gao, C.-M. Jian, and H. Zhai, Spin-orbit coupled spinor Bose-Einstein condensates, Phys. Rev. Lett. **105**, 160403 (2010).

[27] C. Wu, I. Mondragon-Shem, and X.-F. Zhou, Unconventional Bose-Einstein condensations from spin-orbit coupling, Chin. Phys. Lett. **28**, 097102 (2011).

[28] T.-L. Ho and S. Zhang, Bose-Einstein condensates with spin-orbit interaction, Phys. Rev. Lett. **107**, 150403 (2011).

[29] Y. Zhang, L. Mao, and C. Zhang, Mean-field dynamics of spin-orbit coupled Bose-Einstein condensates, Phys. Rev. Lett. **108**, 035302 (2012).

[30] H. Hu, B. Ramachandhran, H. Pu, and X.-J. Liu, Spin-orbit coupled weakly interacting Bose-Einstein condensates in harmonic traps, Phys. Rev. Lett. **108**, 010402 (2012).

[31] T. Ozawa and G. Baym, Stability of ultracold atomic Bose condensates with Rashba spin-orbit coupling against quantum and thermal fluctuations, Phys. Rev. Lett. **109**, 025301 (2012).

[32] Y. Li, L. P. Pitaevskii, and S. Stringari, Quantum tricriticality and phase transitions in spin-orbit coupled Bose-Einstein condensates, Phys. Rev. Lett. **108**, 225301 (2012).

[33] R. Wei and E. J. Mueller, Magnetic-field dependence of Raman coupling in alkali-metal atoms, Phys. Rev. A **87**, 042514 (2013).

[34] Y. Xu, Y. Zhang, and B. Wu, Bright solitons in spin-orbit-coupled Bose-Einstein condensates, Phys. Rev. A **87**, 013614 (2013).

[35] Y. Xu, Y. Zhang, and C. Zhang, Bright solitons in a 2D spin-orbit-coupled dipolar Bose-Einstein condensate, arXiv:1504.06575.

[36] M. Gong, S. Tewari, and C. Zhang, BCS-BEC crossover and topological phase transition in 3D spin-orbit coupled degenerate Fermi gases, Phys. Rev. Lett. **107**, 195303 (2011).

[37] H. Hu, L. Jiang, X.-J. Liu, and H. Pu, Probing anisotropic superfluidity in atomic Fermi gases with Rashba spin-orbit coupling, Phys. Rev. Lett. **107**, 195304 (2011).

[38] Z.-Q. Yu and H. Zhai, Spin-orbit coupled Fermi gases across a Feshbach resonance, Phys. Rev. Lett. **107**, 195305 (2011).

[39] C. Qu, Z. Zheng, M. Gong, Y. Xu, Li Mao, X. Zou, G. Guo, and C. Zhang, Topological superfluids with finite-momentum pairing and Majorana fermions, Nat. Commun. **4**, 2710 (2013).

[40] W. Zhang and W. Yi, Topological Fulde-Ferrell-Larkin-Ovchinnikov states in spin-orbit-coupled Fermi gases, Nat. Commun. **4**, 2711 (2013).

[41] C. Chen, Inhomogeneous topological superfluidity in one-dimensional spin-orbit-coupled Fermi gases, Phys. Rev. Lett. **111**, 235302 (2013).

[42] Y. Xu, C. Qu, M. Gong, and C. Zhang, Competing superfluid orders in spin-orbit-coupled fermionic cold-atom optical lattices, Phys. Rev. A **89**, 013607 (2014).

[43] F. Lin, C. Zhang, and V. W. Scarola, Emergent kinetics and fractionalized charge in 1D spin-orbit coupled flatband optical lattices, Phys. Rev. Lett. **112**, 110404 (2014).

[44] Y. Xu, L. Mao, B. Wu, and C. Zhang, Dark solitons with Majorana Fermions in spin-orbit-coupled Fermi gases, Phys. Rev. Lett. **113**, 130404 (2014).

[45] L. Jiang, E. Tiesinga, X.-J. Liu, H. Hu, and H. Pu, Spin-orbit-coupled topological Fulde-Ferrell states of fermions in a harmonic trap, Phys. Rev. A **90**, 053606 (2014).

[46] Y. Xu and C. Zhang, Berezinskii-Kosterlitz-Thouless phase transition in 2D spin-orbit coupled Fulde-Ferrell superfluids, Phys. Rev. Lett. **114**, 110401 (2015).

[47] Y. Xu and C. Zhang, Topological Fulde-Ferrell superfluids of a spin-orbit coupled Fermi gas, Int. J. Mod. Phys. B **29**, 1530001 (2015).

[48] L. Jiang, C. Qu, and C. Zhang, 1D topological chains with Majorana fermions in 2D non-topological optical lattices, arXiv:1503.01810.

[49] F. Herman, Theoretical investigation of the electronic energy band structure of solids, Rev. Mod. Phys. **30**, 102 (1958).

[50] I. Žutić, J. Fabian, and S. Das Sarma, Spintronics: Fundamentals and applications, Rev. Mod. Phys. **76**, 323 (2004).

[51] K.-P. Marzlin, W. Zhang, and E. M. Wright, Vortex coupler for atomic Bose-Einstein condensates, Phys. Rev. Lett. **79**, 4728 (1997).

[52] M. F. Andersen, C. Ryu, P. Cladé, V. Natarajan, A. Vaziri, K. Helmerson, and W. D. Phillips, Quantized rotation of atoms from photons with orbital angular momentum, Phys. Rev. Lett. **97**, 170406 (2006).

[53] C. Ryu, M. F. Andersen, P. Cladé, V. Natarajan, K. Helmerson, and W. D. Phillips, Observation of persistent flow of a Bose-Einstein condensate in a toroidal trap, Phys. Rev. Lett. **99**, 260401 (2007).

[54] L. S. Leslie, A. Hansen, K. C. Wright, B. M. Deutsch, and N. P. Bigelow, Creation and detection of Skyrmions in a Bose-Einstein condensate, Phys. Rev. Lett. **103**, 250401 (2009)

[55] N. Lo Gullo, S. McEndoo, T. Busch, and M. Paternostro, Vortex entanglement in Bose-Einstein condensates coupled to Laguerre-Gauss beams, Phys. Rev. A **81**, 053625 (2010).

[56] S. Beattie, S. Moulder, R. J. Fletcher, and Z. Hadzibabic, Persistent currents in spinor condensates, Phys. Rev. Lett. **110**, 025301 (2013).

[57] G. Juzeliūnas and P. Öhberg, Slow light in degenerate Fermi gases, Phys. Rev. Lett. **93**, 033602 (2004).

[58] N. R. Cooper and Z. Hadzibabic, Measuring the superfluid fraction of an ultracold atomic gas, Phys. Rev. Lett. **104**, 030401 (2010).

[59] A. Ramanathan, K. C. Wright, S. R. Muniz, M. Zelan, W. T. Hill, C. J. Lobb, K. Helmerson, W. D. Phillips, and G. K. Campbell, Superflow in a toroidal Bose-Einstein condensate: An atom circuit with a tunable weak link, Phys. Rev. Lett. **106**, 130401 (2011).

[60] K. C. Wright, R. B. Blakestad, C. J. Lobb, W. D. Phillips, and G. K. Campbell, Driving phase slips in a superfluid atom circuit with a rotating weak link, Phys. Rev. Lett. **110**, 025302 (2013).

[61] S. Eckel, J. G. Lee, F. Jendrzejewski, N. Murray, C. W. Clark, C. J. Lobb, W. D. Phillips, M. Edwards, and G. K. Campbell, Hysteresis in a quantized superfluid 'atomtronic' circuit, Nature (London) **506**, 200 (2014).

[62] F. Wilczek, Quantum time crystals, Phys. Rev. Lett. **109**, 160401 (2012).

[63] M. Olshanii, Atomic scattering in the presence of an external confinement and a gas of impenetrable bosons, Phys. Rev. Lett. **81**, 938 (1998).

[64] T. Bergeman, M. G. Moore, and M. Olshanii, Atom-atom scattering under cylindrical harmonic confinement: Numerical and analytic studies of the confinement induced resonance, Phys. Rev. Lett. **91**, 163201 (2003).

[65] S. Moulder, S. Beattie, R. P. Smith, N. Tammuz, and Z. Hadzibabic, Quantized supercurrent decay in an annular Bose-Einstein condensate, Phys. Rev. A **86**, 013629 (2012).

[66] J. Stenger, S. Inouye, D. M. Stamper-Kurn, H.-J. Miesner, A. P. Chikkatur, and W. Ketterle, Spin domains in ground-state Bose-Einstein condensates, Nature (London) **396**, 345 (1998).

[67] P.-P. Huang, C.-A. Chen, H.-J. Wei, C.-Y. Yu, J.-B. Wang, and Y.-J. Lin, Towards generating synthetic gauge potentials for a Bose-Einstein condensate in a toroidal trap, DAMOP abstract, http://meetings.aps.org/Meeting/DAMOP15/Session/K1.53 (2015).